Systematic *ab initio* study of the optical properties of BN nanotubes

G. Y. Guo* and J. C. Lin
Department of Physics, National Taiwan University, Taipei, Taiwan 106, Republic of China
(Received 28 November 2004; revised manuscript received 14 January 2005; published 4 April 2005)

A systematic *ab initio* study of the optical and electronic properties of BN nanotubes within density functional theory in the local density approximation is performed. Specifically, the optical dielectric function ε and the band structure of the single-walled zigzag [(5,0),(6,0),(9,0),(12,0),(15,0),(20,0),(27,0)], armchair [(3,3),(4,4),(6,6),(8,8),(12,12),(15,15)], and chiral [(4,2),(6,4),(8,4),(10,5)] as well as the double-walled zigzag (12,0)@(20,0) BN nanotubes are calculated. The underlying atomic structure of the BN nanotubes is determined theoretically. It is found that though the band gap of all the single-walled nanotubes with a diameter larger than 15 Å is independent of diameter and chirality, the band gap of the zigzag nanotubes with smaller diameters decreases strongly as the tube diameters decrease and that of the armchair nanotubes has only a weak diameter dependence, while the band gap of the chiral nanotubes falls in between. It is also found that for the electric field parallel to the tube axis ($E \| \hat{z}$), the absorptive part ε'' of the dielectric function for all the nanotubes except a few with very small diameters, is very similar to that of bulk hexagonal (h) BN with the electric field parallel to the BN layers ($E \perp c$). In other words, in the low-energy region (4–9 eV) the ε'' consists of a single distinct peak at ~5.5 eV, and in the high-energy region (9–25 eV) it exhibits a broad peak centered near 14.0 eV. For the electric field perpendicular to the tube axis ($E \perp \hat{z}$), the ε'' spectrum of all the nanotubes (except the ultrasmall-diameter nanotubes) in the low-energy region also consists of a pronounced peak at ~6.0 eV, while in the high-energy region it is roughly made up of a broad hump starting from 10.0 eV. The magnitude of the peaks is in general less than half of the magnitude of the corresponding ones for $E \| \hat{z}$, showing a moderate optical anisotropy in the nanotubes that is smaller than in *h*-BN. Interestingly, the static dielectric constant $\varepsilon(0)$ for all the nanotubes is almost independent of diameter and chirality with $\varepsilon(0)$ for $E \| \hat{z}$ being only about 30% larger than for $E \perp \hat{z}$. For both electric-field polarizations, the static polarizability $\alpha(0)$ is roughly proportional to the tube diameter, suggesting that, unlike carbon nanotubes, the valence electrons on the BN nanotubes are tightly bound. The calculated electron energy-loss spectra of all the nanotubes studied here for both electric field polarizations are similar to those of $E \perp c$ of *h*-BN, being dominated by a broad $\pi+\sigma$-electron plasmon peak at ~26 eV and a small π-electron plasmon peak at ~7 eV. Interwall interaction is found to reduce the band gap slightly and to have only minor effects on the dielectric functions and energy-loss spectra. The calculated dielectric functions and energy-loss spectra are in reasonable agreement with the available experimental data.

DOI: 10.1103/PhysRevB.71.165402 PACS number(s): 78.67.Ch, 71.20.Nr, 73.22.−f, 77.84.Bw

I. INTRODUCTION

Since their discovery in 1991,[1] carbon nanotubes (CNTs) have attracted considerable interest worldwide because of their unusual properties and great potential for technological applications. For example, because of their one-dimensional character, metallic CNTs are quantum wires that may exhibit exotic Luttinger-liquid behavior rather than the usual Fermi-liquid behavior in normal metal wires.[2] CNTs can be considered as a layer of graphene sheet rolled up into a cylinder, and the structure of a CNT is completely specified by the chiral vector which is given in terms of a pair of integers (n,m).[3] A simple π-band tight-binding model predicts that, depending on the way of rolling up the nanotube, it can be metallic, semiconducting, or insulating.[3] CNTs can be chiral or nonchiral, again depending on the way they are rolled. CNTs are classified into three types, namely, armchair (n,n) nanotubes, zigzag $(n,0)$ nanotubes, and chiral (n,m) nanotubes with $n \neq m$.[3] Because of their one-dimensional character and chirality, chiral CNTs are expected to exhibit a number of unusual optical properties such as optical activity, circular dichroism, and second harmonic generation (see Refs. 4 and 5 and references therein).

Soon after the discovery of CNTs it became obvious that similar nanostructures could be formed by other elements and compounds which form layered structures bearing some resemblance to graphite. For example, hexagonal BN (*h*-BN) was predicted on the basis of theoretical calculations[6,7] to be capable of forming nanotubes, a prediction which was later confirmed experimentally by the synthesis of such nanotubes.[8] Both single-walled and multiwalled BN nanotubes (BN-NTs) can now be readily synthesized.[9] Though CNTs continue to attract great interest, other nanotubes such as BN-NTs are interesting in their own right and may be able to offer different possibilities for technological applications that CNTs cannot provide. In particular, as far as the optical and optoelectronic applications of nanotubes are concerned, BN-NTs could be superior to CNTs because BN-NTs are uniformly insulating, independent of their chirality. Furthermore, BN-NTs tend to have a zigzag structure.[9] Though it is interesting that CNTs can be metallic, semiconducting, or insulating, it is still impossible to grow CNTs with a prespecified chirality at present. Finally, recent experiments indicate that BN-NTs exhibit a stronger resistance to oxidation at high temperatures than CNTs.[10]

Therefore, the electronic, optical, and other properties of both single-walled and multiwalled BN-NTs are interesting and have been intensively studied theoretically in recent years (see, e.g., Refs. 6, 7, and 11–18). In particular, Chen *et al.*[15] calculated the transverse dielectric function of bundles of single-walled BN-NTs using a tight-binding model. Ng and Zhang[18] calculated the optical absorption spectra of single-walled BN-NTs within a time-dependent, localized density-matrix approach based on a semiempirical Hamiltonian. Despite these intensive theoretical studies, only few accurate *ab initio* calculations of the optical properties of BN-NTs have been reported[19] because of the heavy demand on the computing resources. The semiempirical tight-binding model is known to describe well only the electronic excitations near the band gap of the large radius BN-NTs. Systematic *ab initio* calculations of the optical properties are thus needed in order to quantitatively interpret the optical experiments and to predict the BN-NTs with desired optical properties. The primary objective of the present work is to analyze the band structure and optical features of all three types of the BN-NTs and their possible dependence on diameter and chirality through a series of *ab initio* calculations. The second objective is to identify characteristic differences in both electronic and optical properties between BN-NTs and CNTs.

The rest of this paper is organized as follows. In Sec. II, the theoretical approach and computational details are briefly described. The theoretically determined structural parameters and the curvature energy of the nanotubes are also reported. In Sec. III, the calculated band structure, density of states, optical dielectric function and electron energy-loss spectrum of *h*-BN, single hexagonal BN sheet, and BN nanotubes are presented and analyzed. Finally, in Sec. IV, a summary is given.

II. THEORY AND COMPUTATIONAL METHOD

Our *ab initio* calculations for the BN-NTs were performed using the highly accurate full-potential projected augmented wave (PAW) method,[20] as implemented in the VASP package.[21] They are based on density functional theory (DFT) with the local density approximation (LDA). A supercell geometry was adopted so that the nanotubes are aligned in a square array with the closest distance between adjacent nanotubes being at least 6 Å. As a test, calculations with larger intertube distances were performed and no discernable differences were found. A large plane-wave cutoff of 450 eV was used throughout. We consider a few representative BN-NTs with a range of diameters from all three types, as listed in Table I.

A. Structural optimization

First, the ideal nanotubes were constructed by rolling up a hexagonal BN sheet. Their atomic positions and lattice constants were then fully relaxed by a conjugate gradient technique. Theoretical equilibrium nanotube structures were obtained when the forces acting on all the atoms and the uniaxial stress were less than 0.03 eV/Å and 2.0 kBar, respectively. In these atomic structure optimizations, a uniform grid $(1\times1\times n)$ along the nanotube axis (z axis) with the number n of the k points ranging from 12 to 50, was used. The special k-point method plus Gaussian broadening technique was used for the Brillouin zone integration. The theoretical equilibrium lattice constants T and curvature energies E_c (total energy relative to that of a single BN sheet) (also known as the strain energies) as well as the ideal nanotube diameters D are listed in Table I. Note that for the nanotubes with a moderate diameter ($\geqslant$10 Å), the equilibrium structures are already found to be almost the same as that of the ideal nanotubes constructed by rolling up a BN sheet with a B–N bond length of 1.435 Å. This is consistent with the fact that the calculated E_c of the nanotubes with such a diameter is already smaller than 0.05 eV/atom (Table I). Interestingly, as for CNTs, the calculated E_c of BN-NTs can be very well fitted with an expression of $E_c=\alpha/R^2$ with $\alpha=1.248$ eV(Å^2/atom) (see Fig. 1), indicating that the conventional elastic theory works well, even down to such a small length scale. It is gratifying that this diameter dependence of the curvature is in good quantitative agreement with that from previous LDA calculations for the zigzag BN-NTs.[14] Furthermore, as for CNTs, the calculated E_c of BN-NTs are independent of chirality, i.e., all three types of BN-NTs with the same diameter would have the same structural stability. Experimentally, unlike CNTs, BN-NTs produced by laser heating or other methods[9] have a preferred zigzag configuration. Therefore, since Fig. 1 shows that the zigzag BN-NTs are not energetically more favorable, the ob-

TABLE I. Theoretical structural parameters and curvature energy of the BN nanotubes studied. D is the diameter, T is the length of translational vector, N is the number of atoms per unit cell, and E_c is the curvature energy (see text). Note that D is the diameter of the ideal BN nanotubes constructed assuming a B–N bond length of 1.435 Å.

	D (Å)	T (Å)	N	E_c (eV/*atom*)
(5,0)	3.96	4.27	20	0.333
(6,0)	4.75	4.29	24	0.233
(9,0)	7.12	4.30	36	0.103
(12,0)	9.49	4.30	48	0.058
(15,0)	11.87	4.31	60	0.038
(20,0)	15.82	4.30	80	0.021
(27,0)	21.36	4.31	108	0.011
(3,3)	4.11	2.49	12	0.293
(4,4)	5.48	2.49	16	0.169
(5,5)	6.85	2.49	20	0.110
(6,6)	8.22	2.49	24	0.077
(8,8)	10.96	2.49	32	0.044
(12,12)	16.44	2.49	48	0.019
(15,15)	20.55	2.49	60	0.013
(4,2)	4.19	11.41	56	0.290
(6,2)	5.70	15.52	104	0.160
(8,4)	8.37	11.40	112	0.075
(10,5)	10.46	11.40	140	0.049

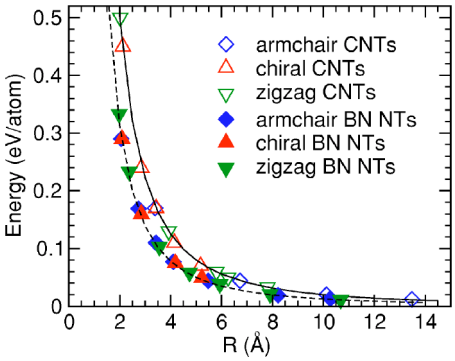

FIG. 1. (Color online) Calculated curvature energies [total energy relative to that of a single BN (graphene) sheet] of BN (carbon) nanotubes. The results for carbon nanotubes are taken from Ref. 4 and the lines are a fitting of α/R^2 to the data sets with $\alpha = 2.004$ and 1.248 eV Å^2/atom for BN and carbon nanotubes, respectively.

served preferential growths of the zigzag BN-NTs have to be due to some other factors such as the larger binding energy of the zigzag BN strips, as speculated by Xiang *et al.*[17]

B. Band structure calculation

The self-consistent electronic band structure calculations were then carried out for the theoretically determined BN-NT structures. In these self-consistent calculations, a denser k-point grid was used and n ranges from 40 to 80. The density of states (DOS) was evaluated from the self-consistent band structure by Gaussian broadening method, i.e.,

$$N(\epsilon) = \sum_n \sum_{\mathbf{k}} w_{\mathbf{k}} \delta(\epsilon - \epsilon_{\mathbf{k}n}), \tag{1}$$

where the Dirac delta function $\delta(x)$ is approximated by a Gaussian function,

$$\delta(x) \approx \frac{1}{\sqrt{\pi}\Gamma} e^{-x^2/\Gamma^2}, \tag{2}$$

$w_{\mathbf{k}}$ is the weight associated with k point $\mathbf{k}$ and $\epsilon_{\mathbf{k}n}$ is the nth energy band. Here the Gaussian width Γ is set to 0.05 eV. An even denser k-point grid along the z axis was used ($n \sim 40$–300) for DOS calculations.

C. Calculation of the optical properties

In this work, the optical properties were calculated based on the independent-particle approximation, i.e., the excitonic effects and the local-field corrections were neglected. As will be shown below, the dielectric functions of h-BN calculated within the single-electron picture are in reasonably good agreement with experiments. Therefore, it might be expected that the independent-particle approximation could work rather well for the BN-NTs too.

The imaginary part of the dielectric function $\varepsilon(\omega)$ due to direct interband transitions is given by the Fermi golden rule (see, e.g., Ref. 4) (atomic units are used in the rest of this paper), i.e.,

$$\varepsilon''_{aa}(\omega) = \frac{4\pi^2}{\Omega\omega^2} \sum_{i \in VB, j \in CB} \sum_{\mathbf{k}} w_{\mathbf{k}} |p^a_{ij}|^2 \delta(\epsilon_{\mathbf{k}j} - \epsilon_{\mathbf{k}i} - \omega), \tag{3}$$

where Ω is the unit cell volume, and ω is the photon energy. Also, VB and CB denote the valence and conduction bands, respectively. The dipole transition matrix elements $p^a_{ij} = \langle \mathbf{k}j | \hat{p}_a | \mathbf{k}i \rangle$ were obtained from the self-consistent band structures within the PAW formalism.[22] Here $|\mathbf{k}n\rangle$ is the nth Bloch state wave function with crystal momentum $\mathbf{k}$, and a denotes the Cartesian component. The real part of the dielectric function is obtained from $\varepsilon''(\omega)$ by a Kramer-Kronig transformation,

$$\varepsilon'(\omega) = 1 + \frac{4}{\pi} \mathrm{P} \int_0^\infty d\omega' \frac{\omega' \varepsilon''(\omega')}{\omega'^2 - \omega^2}. \tag{4}$$

Here P denotes the principal value of the integral. Given the complex dielectric function $(\varepsilon' + i\varepsilon'')$, all other linear optical properties such as refractive index, reflectivity, and absorption spectrum can be calculated. Furthermore, the electron energy-loss spectrum at the long wavelength limit is $-\mathrm{Im}[(\varepsilon' + i\varepsilon'')^{-1}]$ and the electric polarizability α is given by $\varepsilon'(\omega) = 1 + 4\pi\alpha(\omega)/\Omega$.

In the present calculations, the δ-function in Eq. (3) is again approximated by a Gaussian function [Eq. (2)] with $\Gamma = 0.2$ eV. The same k-point grid as in the DOS calculation is used. Furthermore, to ensure that ε' calculated via the Kramer-Kronig transformation [Eq. (4)] is reliable, at least ten energy bands per atom are included in the present optical calculations. The unit cell volume Ω in Eq. (3) is not well defined for nanotubes. Therefore, as in the previous calculations,[4,5] we used the effective unit cell volume of the nanotubes rather than the volume of the supercells, which is arbitrary. The effective unit cell of a nanotube is given by $\Omega = \pi[(D/2 + d/2)^2 - (D/2 - d/2)^2]T$ where d is the thickness of the nanotube cylinder, which is set to the interlayer distance of h-BN (3.28 Å, see Sec. III). D and T are the diameter and length of the translational vector of the nanotube (Table I), respectively. Note that the effective unit cell volume used would not affect the shape and energy position of the features in the optical dielectric functions, though it would change the magnitude of the dielectric function as can be seen from Eq. (3). However, the energy position of the plasmon peaks in the electron energy-loss spectra would be affected by the unit cell volume used. For example, a smaller unit cell volume would shift the energy position of a plasmon peak to a higher energy.

III. RESULTS AND DISCUSSION

A. Hexagonal BN and the single BN sheet

In order to access the accuracy of the present independent-particle approach to the optical properties of the BN structures and also for comparison with the BN-NTs, we first calculated the self-consistent band structure and also the dielectric function for both h-BN and an isolated honeycomb

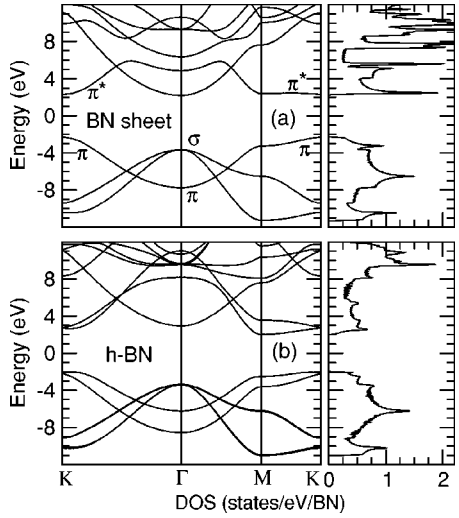

FIG. 2. Energy bands and density of states of *h*-BN and the single BN sheet. The mid-gap energy level is at 0 eV.

BN sheet. The isolated BN sheet is simulated by a slab-supercell approach with an intersheet distance of 6.5 Å. The theoretically determined lattice constants ($a=2.486$ Å and $c=6.562$ Å for *h*-BN and $a=2.485$ Å for the BN sheet) were used. Note that the theoretical lattice constants of *h*-BN agree rather well (within 1.5%) with the experimental values ($a=2.50$ Å and $c=6.65$ Å)[23] and previous LDA calculations (see Refs. 24 and 25 and references therein).

The calculated band structure and density of states of an isolated BN and bulk *h*-BN are displayed in Fig. 2. The band structure of *h*-BN has been calculated and analyzed before (see, e.g., Refs. 26 and 27) and the band structure shown in Fig. 2 is very similar to those reported previously.[26,27] The band structure of the isolated BN sheet also agrees very well with previous LDA calculations.[7] Nevertheless, to facilitate the discussions below, we briefly summarize the salient features of the present band structure of an isolated BN sheet and *h*-BN. Both the upper valence band and the lower conduction band are predominantly of B and N p character. For the single BN sheet, the upper valence band consists of one π band which arises from the $2p_z$ orbitals, extending above and below the BN-layer plane and two σ bands involving the three $(2s,2p_x,2p_y)$ orbitals, which form the coplanar σ bonds joining one B (N) atom to its three N (B) neighbors within the layer [Fig. 2(a)]. Note that the other σ band of mainly the $2s$ character lies about 4.6 eV below the bottom of the upper two σ bands and is not shown in Fig. 2(a). The low-lying conduction bands ranging from 2.2 eV to 5.7 eV are predominantly of the $2p_z$ character, indicating that they are the π^* bands. From about 7.7 eV upwards, the partial density of states of $2s,2p_x,2p_y$ orbitals also becomes significant, suggesting that there are both σ^* and π^* bands in this energy range. There is a direct band gap of 4.5 eV at the K point in the Brillouin zone separating the π and π^* bands. The band structure of *h*-BN is similar to that of the single BN sheet [see Figs. 2(a) and 2(b)]. The differences are that the number of bands in *h*-BN is now doubled and due to interlayer interactions, the double-degenerate π and π^* bands split significantly. The band gap is now reduced to 4.1 eV and becomes indirect.

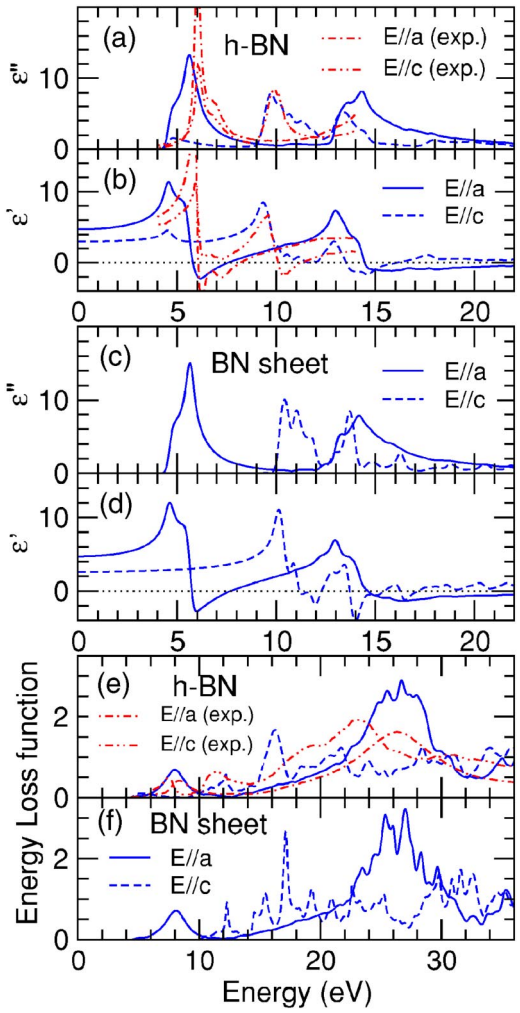

FIG. 3. (Color online) Theoretical dielectric function (a)–(d) and energy-loss function (e)–(f) of the single BN sheet and *h*-BN. For comparison, the experimental (exp.) (from Ref. 28 and references therein) dielectric function and energy loss function of *h*-BN are also shown. The solid and dashed lines represent the theoretical results for the electric field parallel to the BN layers ($E\|a$) and perpendicular to the BN layers ($E\|c$), respectively. The dot-dashed and double-dot-dashed lines denote the experimental spectra for $E\|a$ and $E\|c$, respectively. The dotted lines denote the zero value of the real part (ε') of the dielectric function.

The calculated dielectric function $\varepsilon(\omega)$ and electron energy-loss function of an isolated BN sheet and bulk *h*-BN are shown in Fig. 3. In the calculations, a k-point grid of $60\times60\times16$ for *h*-BN and $100\times100\times2$ for the honeycomb BN sheet is used. The measured $\varepsilon(\omega)$ and also the energy-loss function of *h*-BN (Ref. 28) are also plotted in Fig. 3. Here we summarize the main features in the optical spectra which are relevant to the discussions below.

The optical properties of the single BN sheet and *h*-BN can be conveniently divided into two spectral regions. In the low-energy range from 4.5 eV (the absorption edge) to 9.0 eV, the interband optical transitions involve mainly the π bands. At higher energies, optical absorption features between 11 and 15 eV [see Figs. 3(a) and 3(c)] are associated with interband transitions involving the σ bands. Strong an-

isotropy in the optical spectra can be expected, as demonstrated in Fig. 3, because of distinct optical selection rules. In particular, for a single BN sheet, only $\pi \rightarrow \pi^*$ and $\sigma \rightarrow \sigma^*$ transitions are allowed if the electric field vector **E** is polarized parallel to the BN layer ($E \| \hat{a}$) while, in contrast, only $\pi \rightarrow \sigma^*$ and $\sigma \rightarrow \pi^*$ transitions are allowed if the electric field vector **E** is polarized perpendicular to the BN layer ($E \| \hat{c}$). This is why there is a strong absorption peak at ~5.6 eV for $E \| \hat{a}$ [Figs. 3(a) and 3(c)]. For the single BN sheet, there is no optical absorption for $E \| \hat{c}$ in the low-energy region [Fig. 3(c)]. The very weak absorption in the low-energy region for $E \| \hat{c}$ in Fig. 3(a) is caused by weak interaction between the BN layers in *h*-BN.

For $E \| \hat{a}$, two prominent peaks are found in the energy-loss function, $-\mathrm{Im}\,\epsilon^{-1}$ [Figs. 3(e) and 3(f)]. A small one at ~8.0 eV has been attributed to the collective excitation of π electrons partially screened by the σ electrons. A large broad resonance near 26.0 eV is associated with plasma oscillations involving both the π and σ electrons. On the other hand, for $E \| \hat{c}$, there is no distinct peak at ~8.0 or ~26.0 eV. There are instead many weak resonances in the energy range from 10.0 eV (5.0 eV for *h*-BN) upwards [Figs. 3(e) and 3(f)].

Figure 3 shows that for $E \| \hat{a}$, there is an overall good agreement between the calculated and measured dielectric function and energy-loss function for *h*-BN, suggesting that the many-body effects, such as local-field corrections, are small and hence the present LDA plus independent-particle approach is perhaps rather adequate for describing the optical properties of *h*-BN and other graphitic BN materials. This is further corroborated by the fact that the dielectric function for $E \| \hat{a}$ for the single BN sheet from more advanced time-dependent (TD) DFT-LDA calculations,[19] which include local-field effects and other many-body exchange correlations, is in excellent agreement with the present result [Fig. 3(c)]. Nevertheless, differences between the calculated and measured $\varepsilon(\omega)$ do exist. For example, the prominent low-energy peak in the measured ε'' spectrum appears at a higher energy of 6.1 eV, compared with the theoretical energy of 5.6 eV. However, the energy difference of ~0.5 eV is not large. This is presumably due to the well known fact that DFT-LDA calculations often underestimate the band gaps and transition energies. On the other hand, the so-called quasi-particle *GW* calculations usually give the band-gap values which are in much better agreement with experiments (see, e.g., Ref. 29 and references therein). The band gap of *h*-BN from previous *GW* calculations[29] is 5.4 eV, being larger than the DFT-LDA value of 4.1 eV from the present and previous calculations. This implies that the quasiparticle correction to the LDA energy gap and transition energy is ~1.3 eV, being significantly larger than 0.5 eV. This discrepancy in principle could be resolved once the precise experimental gap of *h*-BN were known. Unfortunately, despite many experiments on *h*-BN (see Ref. 30 and references therein), no consensus concerning the size and nature of the band gap of *h*-BN has been reached. The measured values of the *h*-BN band gap are widely dispersed in the range between 3.6 and 7.1 eV.[30] Further accurate experiments on good single crystals may be necessary to resolve this problem.

For $E \| \hat{c}$, the agreement between the calculated and measured dielectric function and energy-loss function for *h*-BN is not very good. In particular, there is a prominent peak at ~6.1 eV in the measured ε'' spectrum which is absent in the corresponding theoretical spectrum [Fig. 3(a)]. This pronounced discrepancy is perhaps due to the fact that the dielectric function plotted in Fig. 3 was derived from the electron energy-loss spectra (EELS) measurements[28] in which the electric field may have a significant $E \| \hat{a}$ component. This suggestion is further supported by the fact that, as mentioned before, the optical selection rules would forbid strong absorptions for $E \| \hat{c}$ in this low-energy region. Direct optical measurements on good crystals with precise electric field polarizations relative to the crystal axes are therefore needed. Nevertheless, the measured features in the dielectric function in the high-energy region (9.0–15.0 eV) are quite well reproduced by the present theoretical calculations.

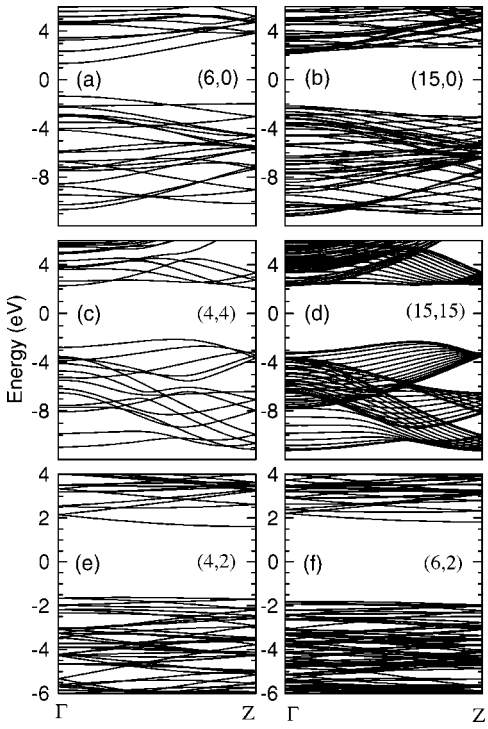

FIG. 4. Energy bands of the representative zigzag, armchair, and chiral BN nanotubes. The midgap energy level is at 0 eV. Note that the length of the Brillouin zone (line ΓZ), which is π/T where T is the lattice constant (Table I), is different for the different nanotubes.

B. Band structure of nanotubes

The energy bands of the three types of BN-NTs studied here are shown in Fig. 4. Only two representative BN-NTs from each type, namely, (6,0) and (15,0) zigzag, (4,4) and (15,15) armchair, and (4,2) and (6,2) chiral nanotubes are selected for display. As expected, all the calculated band structures of the BN-NTs are semiconductors. Interestingly, all the zigzag BN-NTs have a direct band gap, while, in contrast, all the armchair and chiral BN-NTs have an indirect band gap (Fig. 4). The calculated band gaps of all the BN-NTs studied are listed in Table II and also displayed in Fig. 5 as function of their diameters. Figure 5 indicates that, in general, the band gaps of all the BN-NTs increase with

TABLE II. Calculated band gap E_g, static dielectric constant $\varepsilon(0)$, and polarizability $\alpha(0)$ per unit length for the BN nanotubes studied in this work. $D(I)$ denotes direct (indirect) band gap. For comparison, the calculated band gap E_g, and static dielectric constant $\varepsilon(0)$ for the hexagonal BN sheet and hexagonal BN are also listed.

	E_g (eV)	$\varepsilon_{xx}(0)[\varepsilon_{zz}(0)]$	$\alpha_{xx}(0)[\alpha_{zz}(0)]$ (Å)^2
(5,0)	2.10(D)	3.55(4.94)	8.5(13.2)
(6,0)	2.68(D)	3.56(4.86)	10.8(16.2)
(9,0)	3.68(D)	3.58(4.72)	15.3(22.1)
(12,0)	4.10(D)	3.58(4.72)	20.4(29.4)
(15,0)	4.30(D)	3.59(4.69)	25.6(36.5)
(20,0)	4.48(D)	3.50(4.66)	32.9(48.2)
(27,0)	4.56(D)	3.59(4.69)	46.1(65.6)
(4,4)	4.22(I)	3.66(4.53)	12.1(16.1)
(6,6)	4.37(I)	3.64(4.60)	18.1(24.6)
(8,8)	4.54(I)	3.57(4.59)	23.5(32.8)
(12,12)	4.57(I)	3.60(4.63)	35.6(49.7)
(15,15)	4.57(I)	3.57(4.61)	44.0(61.8)
(4,2)	3.23(I)	3.67(4.60)	9.3(12.6)
(6,2)	3.64(I)	3.57(4.64)	12.2(17.3)
(8,4)	4.25(I)	3.56(4.61)	17.8(25.2)
(10,5)	4.40(I)	3.57(4.61)	22.4(31.4)
h-BN	4.07(I)	4.72(3.05)	
BN-sheet	4.52(I)	4.78(2.66)	

their diameters and approach the band gap of the isolated BN sheet when their diameters are larger than 15 Å. The reduction of the band gap relative to that of the BN sheet is caused by the so-called curvature effects.[7,14] When a honeycomb BN sheet is rolled up to form a nanotube, π- and σ-orbitals are no longer orthogonal to each other, and they now can hybridize. This hybridization of the π- and σ-orbitals would modify the band structure obtained by rolling up a BN sheet to form a nanotube. However, the reduction of the band gap for the armchair BN-NTs is rather small (within 8%) (Fig. 5 and Table II). On the other hand, the reduction of the band gap for the chiral BN-NTs is large (up to 29%) and monotonic (Fig. 5 and Table II). The largest reduction of the band gap occurs in the zigzag BN-NTs. This reduction can be as large as 54% and is also monotonic. Since the grown BN-NTs are usually in the zigzag structure, this strong diameter dependence of the band gap can perhaps be used to control the band gap of the BN-NTs by growing the BN-NTs with a prespecified diameter.

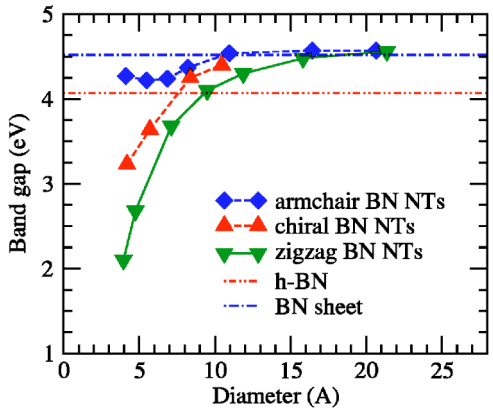

FIG. 5. (Color online) Calculated band gaps of the BN nanotubes vs their tube diameters. For comparison, the band gaps of h-BN and also the single BN sheet are also shown as dash-dotted and dash-double-dotted horizontal lines, respectively.

The present band structures for the (4,4) and (15,0) BN-NTs agree very well with previous LDA calculations from Refs. 7 and 14, respectively. The calculated band gaps are also in good agreement with previous LDA calculations.[14,17] For example, the band gaps for the zigzag (5,0), (9,0), and (15,0) BN-NTs in Ref. 14 are, respectively, 2.4, 3.8, and 4.4 eV, being close to the corresponding values from the present calculations (Table II). The band gaps for the (5,0) and (15,0) from Ref. 17 are, respectively, 2.0 and 4.3 eV, being again in good agreement with the corresponding values in Table II. The strong diameter dependence of the band gap of the zigzag BN-NTs in Fig. 5 has also been found in previous LDA calculations[14,17] while the weak diameter dependence of the band gap of the armchair BN-NTs has been reported in Ref. 17. However, previous semiempirical tight-binding calculations predicted that both the armchair and zigzag BN-NTs have a strong diameter dependence of the band gap,[6] suggesting the importance of the *ab initio* calculations.

The density of states (DOS) of the representative zigzag BN-NTs are shown in Fig. 6. The large diameter (say, $D > 10$ Å) BN-NTs have a very similar DOS spectrum. There are very sharp van Hove singularity peaks in the DOS spectra of small diameter BN-NTs, e.g., the (6,0) (Fig. 6). Another discernable difference is that the band gap becomes

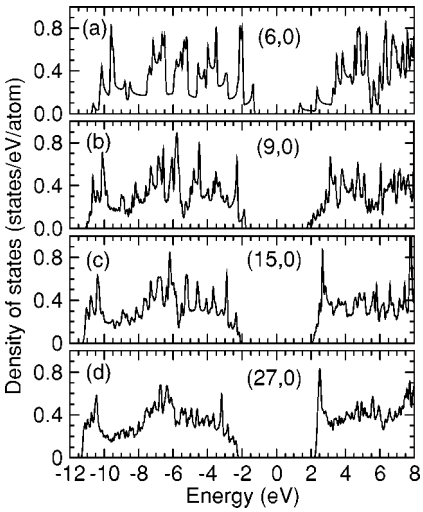

FIG. 6. Density of states of the representative zigzag BN nanotubes. The midgap energy level is at 0 eV.

smaller as the diameter of the BN-NTs decreases, as mentioned before. The DOS of the representative armchair and chiral BN-NTs are displayed in Fig. 7. It is clear that the DOS for the chiral BN-NTs vary quite noticeably with the tube diameter. On the other hand, the DOS of the three armchair BN-NTs look rather similar.

C. Dielectric constant and static polarizability

Figures 8–10 display, respectively, the calculated dielectric function for the representative zigzag [(6,0), (9,0), (15,0), and (27,0)], armchair [(4,4), (6,6), (8,8), and (15,15)], and chiral [(4,2), (6,2), (8,4), and (10,5)] BN-NTs. The spectra can be roughly divided into two regions, namely, the low-energy one from 4 to 9 eV and the high-energy one from 9 to 20 eV. Below about 4 eV (the band-gap region), the ε'' is zero and ε' tends to a constant as the photon energy ap-

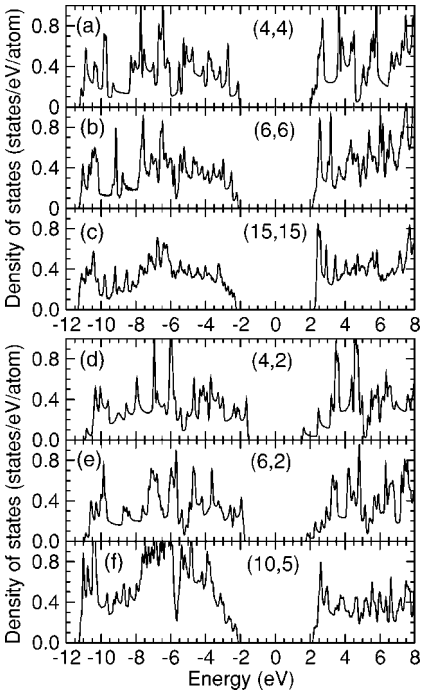

FIG. 7. Density of states of the representative armchair and chiral BN nanotubes. The midgap energy level is at 0 eV.

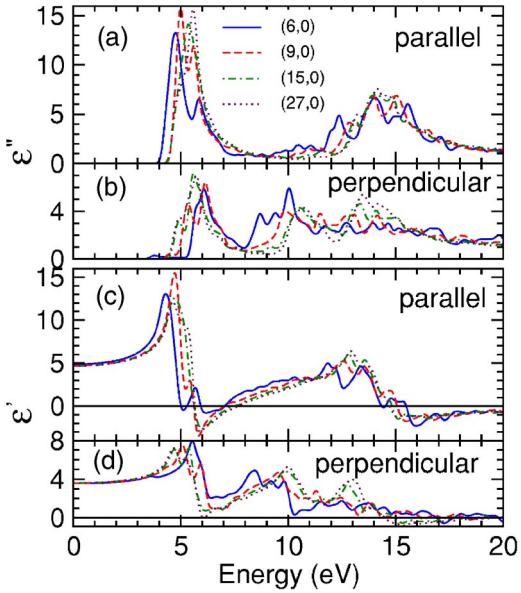

FIG. 8. (Color online) Calculated dielectric function of the zigzag BN nanotubes. "Parallel" and "perpendicular" denote electric fields polarized parallel and perpendicular to the nanotube axis, respectively. The solid, dashed, dot-dashed, and dotted lines represent the dielectric functions for the (6,0), (9,0), (15,0), and (27,0) BN nanotubes, respectively.

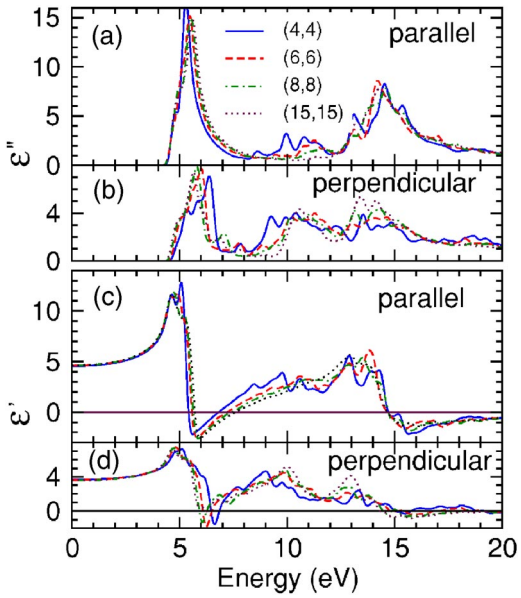

FIG. 9. (Color online) Calculated dielectric function of the armchair BN nanotubes. "Parallel" and "perpendicular" denote electric fields polarized parallel and perpendicular to the nanotube axis, respectively. The solid, dashed, dot-dashed, and dotted lines represent the dielectric functions for the (4,4), (6,6), (8,8), and (15,15) BN nanotubes, respectively.

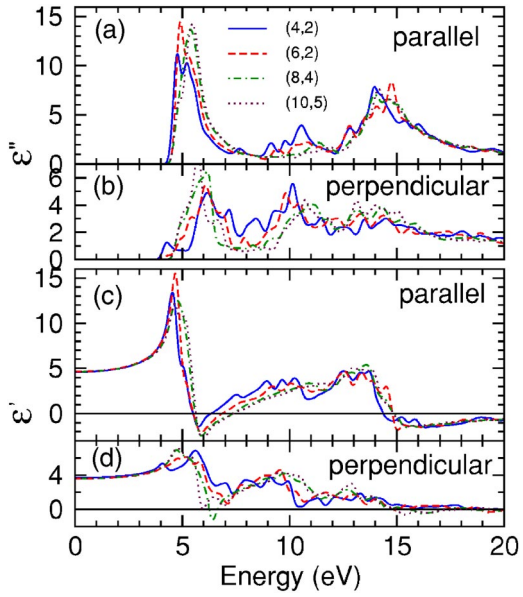

FIG. 10. (Color online) Calculated dielectric function of the chiral BN nanotubes. "Parallel" and "perpendicular" denote electric fields polarized parallel and perpendicular to the nanotube axis, respectively. The solid, dashed, dot-dashed, and dotted lines represent the dielectric functions for the (4,2), (6,2), (8,4), and (10,5) BN nanotubes, respectively.

proaches zero. For the electric field parallel to the tube axis ($E\|\hat{z}$), the ε'' for all three types of the BN-NTs with a moderate diameter (say, $D>10$ Å for the zigzag BN-NTs, and $D>8$ Å for the chiral BN-NTs) in the low-energy region consists of a single distinct peak (Figs. 8–10) at ~5.5 eV. This is in strong contrast to the case of the CNTs in which the distinct features have been found especially for the semiconducting chiral nanotubes[4] and these features can be used to characterize the chirality of the grown carbon nanotubes by optical means.[31,32] However, for small diameter BN nanotubes, the ε'' spectrum does deviate markedly from the general behavior described above (see Figs. 8–10). For example, for the zigzag (6,0) nanotube, the ε'' spectrum exhibits two prominent peaks in the low-energy region at 4.8 and 5.9 eV, respectively [Fig. 8(a)]. For the zigzag (9,0) nanotube, one can also see the two peaks at 5.0 and 5.7 eV, respectively, with a smaller peak separation of about 0.7 eV. The chiral (4,2) and (6,2) nanotubes also have a two-peak structure in the ε'' in the low-energy region [Fig. 10(a)]. In the case of the armchair BN nanotubes, however, only the ε'' spectrum of the ultrasmall-diameter (4,4) BN nanotubes shows a pronounced deviation from that of the rest of the armchair nanotubes. In the high-energy region, the ε'' for all the types of the BN-NTs exhibit a broad peak at ~14.0 eV.

For the electric field perpendicular to the tube axis ($E\perp\hat{z}$), the ε'' spectrum of all the BN-NTs, except the ultrasmall-diameter BN-NTs such as the (4,2), (6,0), and (4,4) nanotubes, in the low-energy region also consists of a pronounced peak at around 6.0 eV, while in the high-energy region it is, roughly, made up of a broad hump starting from 10.0 eV (Figs. 8–10). The magnitude of the peaks is in general about half of the magnitude of the corresponding ones

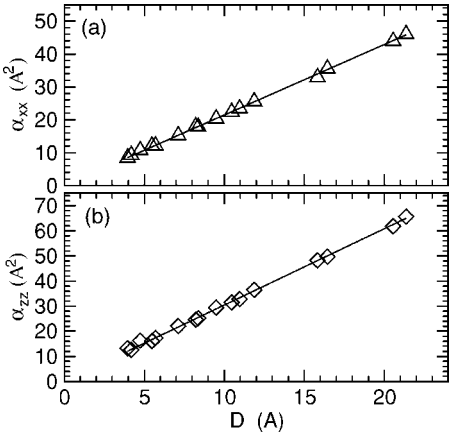

FIG. 11. (a) $\alpha_{xx}(0)$ and (b) $\alpha_{zz}(0)$ vs D for the BN nanotubes studied. The solid line is a linear least-squares fit.

for $E\|\hat{z}$, showing a moderate optical anisotropy in the BN-NTs. In nanotubes, the electric field perpendicular to the nanotube axis is in general strongly screened,[33–35] and this is known as the depolarization effect which is not taken into account in the present calculations. The depolarization effect would substantially reduce the magnitude of the ε'' spectrum for $E\perp\hat{z}$,[19] and hence enhance the optical anisotropy.

Ab initio calculations on the optical properties of BN-NTs have been reported by Marinopoulos *et al.*[19] In Ref. 19, both DFT-LDA and TD-DFT-LDA approaches were adopted. However, the calculations were carried out only for the (3,3), (5,5), and (6,0) BN-NTs of a small diameter because of the numerical demands of the TD-DFT-LDA method. Anyway, the ε'' spectrum of the (6,0) BN-NT for $E\|\hat{z}$ from Ref. 19 is nearly identical to that from the present calculations [Fig. 8(a)], indicating that the local field and other many-body effects are negligible in this case. However, as mentioned before, due to depolarization (local-field) effect, the magnitude of the ε'' spectrum for $E\perp\hat{z}$ from the TD-DFT-LDA calculations is considerably smaller than that from the DFT-LDA calculations.[19]

Let us now compare the dielectric function of the BN-NTs with those of *h*-BN and also a single BN sheet. It is clear from Fig. 3 and Figs. 8–10 that the ε'' spectrum for $E\|\hat{z}$ of the BN-NTs is very similar to that of *h*-BN and the single BN sheet for $E\perp c$. This should be particularly true for the large or even moderate diameter BN-NTs in which the curvature effect is small. This can be expected because the electric field polarization is parallel to the BN layers in both cases. In contrast, the ε'' spectrum for $E\perp\hat{z}$ is rather different from that of $E\perp c$ of *h*-BN and the single BN sheet. In particular, the ε'' spectrum for $E\perp c$ for the photon energy below 9.0 eV is zero in the single BN sheet and very small in *h*-BN (Fig. 3), while in contrast, the ε'' spectrum for $E\perp\hat{z}$ of the BN-NTs has a pronounced peak at ~6.0 eV (Figs. 8–10). This perhaps can be explained as follows. When $E\perp\hat{z}$, it is clear that for some parts of the tube wall, the electric field is nearly perpendicular to the BN layer, while for the other parts of the tube wall, it is roughly parallel to the BN layer. Therefore, the dielectric function for $E\perp\hat{z}$ may be regarded as a mixture of the dielectric functions for both $E\perp c$ and $E\|c$ of the single BN sheet or *h*-BN. This can be seen from

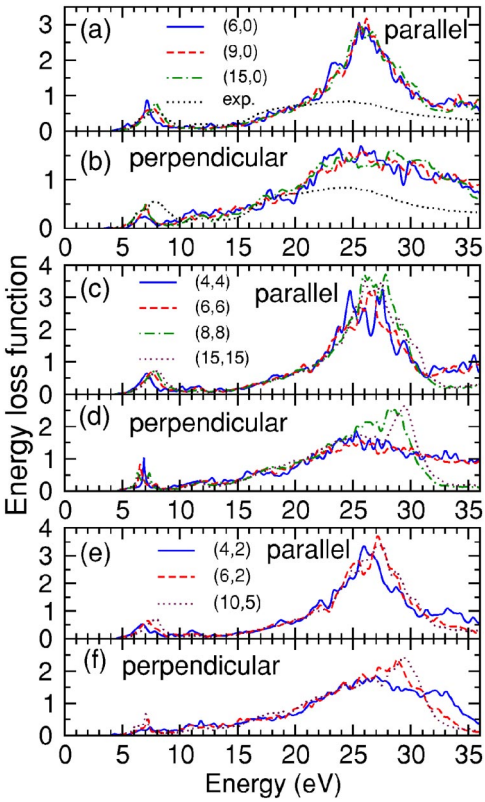

FIG. 12. (Color online) Calculated energy-loss function of the representative BN nanotubes studied. "Parallel" and "perpendicular" denote electric fields polarized parallel and perpendicular to the nanotube axis, respectively. The measured energy-loss function of multiwalled BN nanotubes (Ref. 36) is also plotted in (a) and (b) for comparison.

inspection of Figs. 3 and 8–10, and is particularly clear for large diameter BN-NTs. As a result, it is clear that the calculated optical anisotropy of the large BN-NTs will be smaller than that of the single BN sheet and *h*-BN. Nevertheless, as mentioned before, the depolarization effect $E \perp \hat{z}$ in the BN-NTs may strongly enhance the optical anisotropy of especially small-diameter BN-NTs. Therefore, in optical experiments, one still expects to see a strong optical anisotropy because the ε'' spectrum for $E \perp \hat{z}$ would be substantially reduced due to the depolarization effect.

The static values of the dielectric constant $\varepsilon(0)$ and electric polarizability $\alpha(0)$ of the BN-NTs are listed in Table II. Interestingly, $\alpha(0)$ per unit length for both electric field polarizations is roughly proportional to D (Fig. 11), i.e., $\alpha(0) = a_0 D$, being independent of chirality and electronic structure. For $E \perp \hat{z}$, $a_0 = 2.146$ Å and for $E \| \hat{z}$, $a_0 = 3.041$ Å. This results from the fact that the $\alpha(0)$ per unit length is given by $[\varepsilon'(\omega)-1]\Omega/(4\pi T) = Dd[\varepsilon'(\omega)-1]/4$, and that the $\varepsilon(0)$ is nearly independent of chirality and diameter (Table II). Because the number of atoms on a BN-NT per unit length is proportional to D, this result indicates that every atom on the BN-NT has nearly the same static polarizability. This suggests that the valence electrons in the BN-NTs are tightly bound to the ions, as would be the case for insulators. Strikingly, in recent *ab initio* calculations,[5] it was found that the $\alpha(0)$ per unit length of the CNTs for both electric field polarizations is roughly proportional to D^2. This behavior of $\alpha(0)$ can be understood in an empty lattice model of electrons moving freely on a cylinder of infinitesimal thickness.[34] Therefore, the results of the present and previous *ab initio* $\alpha(0)$ calculations on the BN-NTs and CNTs together suggest that the valence electrons in the BN-NTs behave fundamentally differently from those in the CNTs.

D. Electron energy-loss spectrum

Shown in Fig. 12 are the calculated electron energy-loss spectra (EELS) of some representatives of the zigzag, armchair, and chiral BN-NTs. For $E \| \hat{z}$, the EELS for all the BN-NTs are similar to that of $E \perp c$ of *h*-BN and the single BN sheet [Figs. 3(e) and 3(f)], being dominated by a broad $\pi+\sigma$-electron plasmon peak at 26 eV and a small π-electron plasmon peak at about ~7.5 eV. Nevertheless, the energy positions of the low-energy peaks for very small diameter BN-NTs such as the (4,2), (6,0), and (4,4) are clearly smaller than that of 7.5 eV. Apart from this, the EELS hardly show any chirality dependence.

Unlike the case of $E \| c$ of *h*-BN and the single BN sheet (Fig. 3), the EELS for $E \perp \hat{z}$ are rather similar to the corresponding ones for $E \| \hat{z}$ in shape, but somewhat smaller in amplitude. The weak anisotropy in the EELS of the nanotubes may be attributed to the fact that for $E \perp \hat{z}$ all the $\pi \rightarrow \pi^*$, $\sigma \rightarrow \sigma^*$, $\pi \rightarrow \sigma^*$, and $\sigma \rightarrow \pi^*$ optical transitions are excited, while in *h*-BN and the single BN sheet only $\pi \rightarrow \pi^*$ and $\sigma \rightarrow \sigma^*$ transitions are possible for $E \| c$.

The measured EELS for some multiwalled BN-NTs have been recently reported.[36] Since the BN-NTs tend to grow in the zigzag structure,[9] the EELS for the small momentum transfer $q = 0.1$ Å^{-1} are compared with those of the zigzag BN-NTs in Figs. 12(a) and 12(b). Furthermore, the measured EELS are compared with the theoretical EELS for both $E \| \hat{z}$ and $E \perp \hat{z}$, because the orientation of the momentum transfer q (i.e., the electric field polarization) relative to the tube axis was not known in the experiments. The measured EELS agree rather well with the theoretical ones for $E \| \hat{z}$, especially in the energy range up to 20.0 eV [Fig. 12(a)]. However, pronounced discrepancies between the experiments and the theory appear beyond 20.0 eV. In particular, when compared with the theoretical EELS, the measured high-energy peak is substantially reduced and also shifted to a lower energy (~23.2 eV instead of ~26.0 eV). These large discrepancies are perhaps not due to the fact that here the measured EELS for the multiwalled BN-NTs are compared with the theoretical EELS for the single-walled BN-NTs, because, as will be reported in Sec. III E, interwall interactions hardly have any discernable effects on the calculated EELS. The discrepancies may be in part caused by the fact that close-packed BN nanotube films were used in the experiments[36] while only isolated BN nanotubes are considered in the present calculations. In particular, because of the packing effects, the effective unit cell volume might be larger than the volume we have used, and this would give rise to a shift of the $\pi+\sigma$ plasmon peak to a lower energy. Interestingly, the measured EELS in the high-energy region appears to be in much better

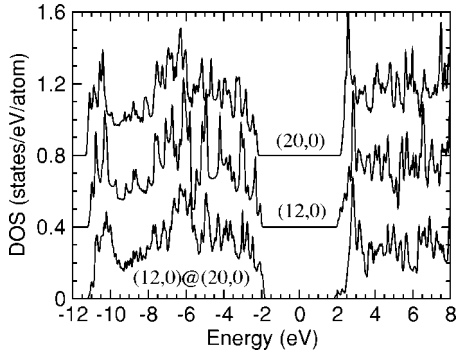

FIG. 13. Calculated density of states (DOS) of the double-walled (12,0)@(20,0) as well as single-walled (12,0) and (20,0) BN nanotubes. The DOS of the (20,0) and (12,0) have been shifted upwards by 0.8 and 0.4 states/eV/atom, respectively. The midgap energy level is at 0 eV.

agreement with the corresponding theoretical ones for $E \perp \hat{z}$ [Fig. 12(b)]. This indicates that the electric field produced by the probing electron beam perhaps has a large $E \perp \hat{z}$ component in the measurements.[36] The EELS for the (6,0) BN-NT for $q \rightarrow 0$ from the TD-DFT-LDA calculations have been recently reported,[19] and they roughly agree with the theoretical EELS from the present calculations. However, the high-energy $\pi+\sigma$ plasmon peak from Ref. 19 appears at a much lower energy (20.0 eV), and this is perhaps due to the use of the arbitrary supercell volume and/or the inclusion of an insufficient number of conduction bands in the previous calculations.[19]

E. Effects of interwall interactions

We have so far focused only on the optical properties of single-walled BN-NTs. However, BN-NTs are usually multiwalled. Therefore, to study the possible effects of interwall interactions on the optical properties of BN-NTs, we have also calculated the electronic structure and dielectric function of a double-walled BN-NT, namely, the zigzag (12,0)@(20,0). This double-walled nanotube is choosen because BN-NTs typically have a zigzag structure, as mentioned before, and also because the interwall distance of about 3.2 Å between the (12,0) and (20,0) nanotubes is close to the interlayer distance in *h*-BN. Again, the theoretically determined atomic structure is used in the electronic structure and optical properties calculations. The calculated formation energy ΔE is 11 meV/atom. The ΔE is given by the sum of the total energies of the (12,0) and (20,0) BN-NTs minus the total energy of the double-walled (12,0)@(20,0) BN-NT. This value is slightly smaller than half of the formation energy of *h*-BN (27 meV/atom). This is reasonable since in *h*-BN each BN layer has two neighboring BN layers, while the (12,0)@(20,0) BN-NT, has only one neighboring BN layer. The ΔE is about 7 meV/atom from the previous LDA calculations,[14] being in rather good agreement with the present calculations.

The calculated density of states of the (12,0)@(20,0) double-walled BN-NT are shown in Fig. 13 together with that of the (12,0) and (20,0) BN-NTs. Figure 13 shows that

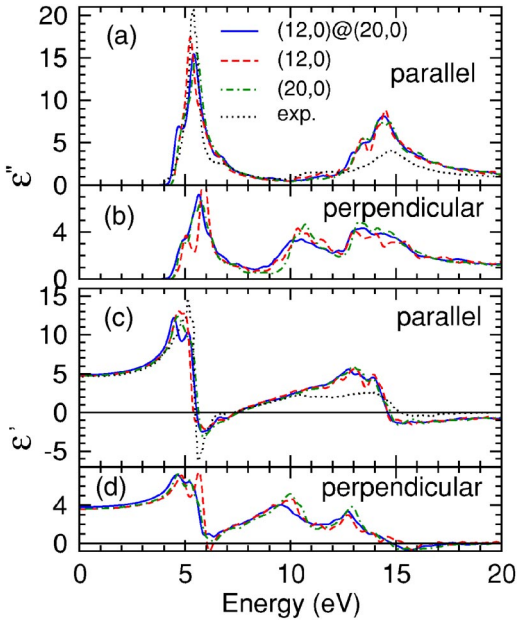

FIG. 14. (Color online) Calculated dielectric function of the double-walled (12,0)@(20,0) (solid lines) as well as single-walled (12,0) (dashed lines) and (20,0) (dot-dashed lines) BN nanotubes. "Parallel" and "perpendicular" denote electric fields polarized parallel and perpendicular to the nanotube axis, respectively. The experimental dielectric function of multiwalled BN nanotubes (Ref. 36) (dotted lines) is also plotted in (a) and (c) for comparison.

the density of states of all three nanotubes are in general very similar, suggesting that the effects of interwall interaction on the electronic structure would be small. Nevertheless, minor differences do exist between the (12,0)@(20,0) and the (12,0) and (20,0). The most obvious difference is that the gap (3.8 eV) of the (12,0)@(20,0) is smaller than that of both the (12,0) (4.1 eV) and (20,0) (4.5 eV) (see Table II). This perhaps can be expected because interlayer interaction causes the gap of *h*-BN to be smaller than that of the single BN sheet by as much as 0.4 eV.

The calculated dielectric function of the (12,0)@(20,0) double-walled BN-NT is shown in Fig. 14 together with those of the (12,0) and (20,0) BN-NTs. The calculated EELS of the (12,0)@(20,0), (12,0), and (20,0) BN-NTs are nearly identical to that of the (9,0) and (15,0) BN-NTs plotted in Figs. 12(a) and 12(b), and therefore are not shown here. Figure 14 indicates that the dielectric functions of all three nanotubes are in general very similar, showing that the effects of interwall interaction on the optical properties would be small. In particular, the dielectric function of the (12,0)@(20,0) is nearly the same as that of the (20,0). Nevertheless, the ε'' for $E \| \hat{z}$ of the (12,0)@(20,0) has two additional shoulders at ~4.6 and 6.9 eV, respectively. As mentioned before, due to the curvature effects, the dielectric function of the (12,0) differs slightly from the larger diameter (20,0). This difference is especially apparent for $E \perp \hat{z}$ in the feature between 4.0–7.0 eV.

The dielectric function of some multiwalled BN-NTs has been derived from the measured EELS spectra by the Kramer-Kronig analysis.[36] Both the imaginary and real parts of the electric function for the small momentum transfer q

$=0.1$ Å^{-1} are plotted in Fig. 14 for comparison with the theoretical ones of the (12,0)@(20,0) BN-NT for $E\|\hat{z}$. Remarkably, there is a very good agreement between experiment and theory [Figs. 14(a) and 14(c)]. In particular, the sharp peak at $\sim$5.4 eV and the small shoulder at 6.8 eV in the experimental ε'' in the low-energy region are very well reproduced by the present calculations. The pronounced differences include that the experimental spectra in the high-energy region have significantly smaller amplitudes compared with the corresponding theoretical ones [Figs. 14(a) and 14(c)]. Furthermore, the shoulder at $\sim$4.6 eV in the ε'' spectrum for $E\|\hat{z}$ predicted by the calculation does not appear on the corresponding experimental spectrum. Interestingly, the shoulder does not appear in the theoretical ε'' spectra for $E\|\hat{z}$ of the (12,0) and (20,0) BN-NTs either [Fig. 14(a)].

IV. SUMMARY

We have carried out a systematic *ab initio* study of the optical as well as structural and electronic properties of the BN-NTs within density functional theory in the local density approximation. Specifically, the properties of the single-walled zigzag [(5,0),(6,0),(9,0),(12,0),(15,0),(20,0),(27,0)], armchair [(3,3),(4,4),(5,5),(6,6),(8,8),(12,12),(15,15)], and chiral [(4,2),(6,2),(8,4),(10,5)] nanotubes as well as the double-walled (12,0)@(20,0) nanotube were calculated. For comparison, the structural, electronic, and optical properties of *h*-BN and the single BN sheet have also been calculated. We find that the calculated lattice constants of *h*-BN are in good agreement with experiments, and that for the electric field parallel to the BN layers, the calculated optical properties of *h*-BN are also in good agreement with experiments. This suggests that the present theoretical approach is perhaps adequate for investigating the optical properties of the BN nanotubes, at least, for the electric field along the tube axis.

We find that though the band gap of the single-walled nanotubes with a diameter larger than 15 Å is independent of diameter and chirality, the band gap of the small diameter zigzag nanotubes decreases, strongly as the tube diameter decreases, and that of the armchair nanotubes has only a weak diameter dependence, while the band gap of the chiral nanotubes falls in between. We also find that as for *h*-BN and also the CNTs, the optical properties of the BN nanotubes can be divided into two spectral regions, namely, the low-energy region (0–9 eV) in which optical transitions involve mainly the π bands and the high-energy region (9–25 eV) in which interband transitions involve mainly the σ bands. For $E\|\hat{z}$, the ε'' for all three types of the BN-NTs with a moderate diameter (say, $D>10$ Å for the zigzag BN-NTs, and $D>8$ Å for the chiral BN-NTs) in the low-energy region consists of a single distinct peak at $\sim$5.5 eV. However, for small-diameter BN nanotubes such as the (6,0),(4,4),(4,2) BN-NTs, the ε'' spectrum does deviate markedly from this general behavior. In the high-energy region, the ε'' for all the types of the BN-NTs exhibit a broad peak centered near 14.0 eV. For $E\perp\hat{z}$, the ε'' spectra of all the BN-NTs, except the ultrasmall diameter BN-NTs such as the (4,2), (6,0), and (4,4) nanotubes, in the low-energy region also consists of a pronounced peak at around 6.0 eV, while in the high-energy region it is roughly made up of a broad hump starting from 10.0 eV. The magnitude of the peaks is in general less than half of the magnitude of the corresponding ones for $E\|\hat{z}$, showing a moderate optical anisotropy in the BN-NTs.

Interestingly, unlike the CNTs, the calculated static dielectric constants $\varepsilon(0)$ for all the nanotubes are almost independent of diameter and chirality with the $\varepsilon(0)$ for $E\|\hat{z}$ being only about 30% larger than for $E\perp\hat{z}$. Remarkably, for both electric-field polarizations, $\alpha(0)$ per unit length is roughly proportional to the tube diameter, being independent of chirality and diameter. This is in strong contrast to the case of the CNTs in which $\alpha(0)$ per unit length is roughly proportional to the square of the tube diameter. This indicates that the nature of the valence electrons in the BN-NTs differs fundamentally from that in the CNTs, namely, the valence electrons on the BN-NTs are tightly bound to the ions, while in the CNTs they behave like free electrons on the cylindrical tubes.

The calculated electron energy-loss spectra of all the BN nanotubes studied here for both electric-field polarizations are similar to that of the $E\perp c$ of *h*-BN, being dominated by a broad $\pi+\sigma$-electron plasmon peak at near 26 eV and a small π-electron plasmon peak at $\sim$7 eV. Thus, the anisotropy is much smaller than that of *h*-BN. Interwall interaction is found to reduce the band gap slightly and to have only minor effects on the optical dielectric functions and electron energy-loss spectra.

ACKNOWLEDGEMENTS

The authors gratefully acknowledge financial support from National Science Council, Ministry of Economic Affairs (Grant No. 92-EC-17-A-08-S1-0006) and NCTS/TPE of the Republic of China. The authors also thank the National Center for High-Performance Computing of the Republic of China for providing CPU time.

*Electronic address: gyguo@phys.ntu.edu.tw

[1] S. Iijima, Nature (London) **354**, 56 (1991).

[2] M. Bockrath, D. H. Cobden, J. Lu, A. G. Rinzler, R. E. Smalley, L. Balents, and P. L. McEuen, Nature (London) **397**, 598 (1999).

[3] R. Saito, G. Dresselhaus, and M. S. Dresselhaus, *Physical Properties of Carbon Nanotubes* (Imperial College, London, 1998).

[4] G. Y. Guo, K. C. Chu, D.-S. Wang, and C.-G. Duan, Phys. Rev. B **69**, 205416 (2004).

[5] G. Y. Guo, K. C. Chu, D.-S. Wang, and C.-G. Duan, Comput. Mater. Sci. **30**, 269 (2004).

[6] A. Rubio, J. L. Corkill, and M. L. Cohen, Phys. Rev. B **49**,

R5081 (1994).
[7] X. Blase, A. Rubio, S. G. Louie, and M. L. Cohen, Europhys. Lett. **28**, 335 (1994)
[8] E.g., N. G. Chopra, R. J. Luyken, K. Cherrey, V. H. Crespi, M. L. Cohen, S. G. Louie, and A. Zettl, Science **28**, 335 (1994); A. Loiseau, F. Willaime, N. Demoncy, G. Hug, and H. Pascard, Phys. Rev. Lett. **76**, 4737 (1996).
[9] R. S. Lee, J. Gavillet, M. Lamy de la Chapelle, A. Loiseau, J.-L. Cochon, D. Pigache, J. Thibault, and F. Willaime, Phys. Rev. B **64**, 121405(R) (2001).
[10] Y. Chen, J. Zou, S. J. Campbell, and G. L. Caer, Appl. Phys. Lett. **84**, 2430 (2004).
[11] O. E. Alon, Phys. Rev. B **64**, 153408 (2001).
[12] Y.-H. Kim, K. J. Chang, and S. G. Louie, Phys. Rev. B **63**, 205408 (2001).
[13] E. J. Mele and P. Kral, Phys. Rev. Lett. **88**, 056803 (2002).
[14] S. Okada, S. Saito, and A. Oshiyama, Phys. Rev. B **65**, 165410 (2002).
[15] R. B. Chen, F. L. Shyu, C. P. Chang, and M. F. Lin, J. Phys. Soc. Jpn. **71**, 2286 (2002).
[16] B. Akdim, R. Pachter, X. Duan, and W. Wade Adams, Phys. Rev. B **67**, 245404 (2003).
[17] H. J. Xiang, J. Yang, J. G. Hou, and Q. Zhu, Phys. Rev. B **68**, 035427 (2003).
[18] M.-F. Ng and R. Q. Zhang, Phys. Rev. B **69**, 115417 (2004).
[19] A. G. Marinopoulos, L. Wirtz, A. Marini, V. Olevano, A. Rubio, and L. Reining, Appl. Phys. A: Mater. Sci. Process. **78**, 1157 (2004).
[20] P. E. Blöchl, Phys. Rev. B **50**, 17953 (1994); G. Kresse and D. Joubert, *ibid.* **59**, 1758 (1999).
[21] G. Kresse and J. Hafner, Phys. Rev. B **47**, R558 (1993); **49**, 14251 (1994); G. Kresse and J. Furthmüller, Comput. Mater. Sci. **6**, 15 (1996).
[22] B. Adolph, J. Furthmüller, and F. Bechsted, Phys. Rev. B **63**, 125108 (2001).
[23] G. Cappellini, V. Fiorentini, K. Tenelsen, and F. Bechstedt, in *Gallium Nitride and Related Materials*, edited by R. D. Dupuis, J. A. Edmond, F. A. Ponce, and S. Nakamura, Materials Research Society Symposia Proceedings No. 395 (Materials Research Society, Pittsburgh, 1996).
[24] G. Cappellini, G. Satta, M. Palummo, and G. Onida, Phys. Rev. B **64**, 035104 (2001).
[25] A. Janotti, S.-H. Wei, and D. J. Singh, Phys. Rev. B **64**, 174107 (2001).
[26] Y.-N. Xu, W. Y. Ching, Phys. Rev. B **44**, 7787 (1991).
[27] L. Liu, Y. P. Feng, and Z. X. Shen, Phys. Rev. B **68**, 104102 (2003).
[28] C. Tarrio and S. E. Schnatterly, Phys. Rev. B **40**, 7852 (1989).
[29] X. Blase, A. Rubio, S. G. Louie, and M. L. Cohen, Phys. Rev. B **51**, 6868 (1995).
[30] V. L. Solozhenko, A. G. Lazarenko, J.-P. Petitet, and A. V. Kanaev, J. Phys. Chem. Solids **62**, 1331 (2001).
[31] Z. M. Li, Z. K. Tang, H. J. Liu, N. Wang, C. T. Chan, R. Saito, S. Okada, G. D. Li, J. S. Chen, N. Nagasawa, and S. Tsuda, Phys. Rev. Lett. **87**, 127401 (2001).
[32] S. M. Bachilo, M. S. Strano, C. Kittrell, R. H. Hauge, R. E. Smalley, and R. B. Wiesman, Science **298**, 2361 (2002).
[33] H. Ajiki and T. Ando, Physica B **201**, 349 (1994); Jpn. J. Appl. Phys., Suppl. **34**, 107 (1995).
[34] L. X. Benedict, S. G. Louie, and M. L. Cohen, Phys. Rev. B **52**, 8541 (1995).
[35] A. G. Marinopoulos, L. Reining, A. Rubio, and N. Vast, Phys. Rev. Lett. **91**, 046402 (2003).
[36] G. G. Fuentes, E. Borowiak-Palen, T. Pichler, X. Liu, A. Graff, G. Behr, R. J. Kalenczuk, M. Knupfer, and J. Fink, Phys. Rev. B **67**, 035429 (2003).